ChemPubSoc Europe

DOI: 10.1002/chem.201704193

CHEMISTRY A European Journal Full Paper

Actinides

Remarkably High Stability of Late Actinide Dioxide Cations: Extending Chemistry to Pentavalent Berkelium and Californium

Phuong D. Dau,[a] Monica Vasiliu,[b] Kirk A. Peterson,*[c] David A. Dixon,*[b] and John K. Gibson*[a]

Abstract: Actinyl chemistry is extended beyond Cm to BkO_2^+ and CfO_2^+ through transfer of an O atom from NO_2 to BkO^+ or CfO^+, establishing a surprisingly high lower limit of 73 kcal mol^{-1} for the dissociation energies, D[O-(BkO^+)] and D[O-(CfO^+)]. CCSD(T) computations are in accord with the observed reactions, and characterize the newly observed dioxide ions as linear pentavalent actinyls; these being the first Bk and Cf species with oxidation states above IV. Computations of actinide dioxide cations AnO_2^+ for An = Pa to Lr reveal an unexpected minimum for D[O-(CmO^+)]. For CmO_2^+, and AnO_2^+ beyond EsO_2^+, the most stable structure has side-on bonded η^2-(O_2), as An^{III} peroxides for An = Cm and Lr, and as An^{II} superoxides for An = Fm, Md, and No. It is predicted that the most stable structure of EsO_2^+ is linear $[O{=}Es^{V}{=}O]^+$, einsteinyl, and that FmO_2^+ and MdO_2^+, like CmO_2^+, also have actinyl(V) structures as local energy minima. The results expand actinide oxidation state chemistry, the realm of the distinctive actinyl moiety, and the nonperiodic character towards the end of the periodic table.

Introduction

Among the most central aspects of metal ion chemistry is the accessibility of oxidation states. This attribute, for example, clearly distinguishes the strictly monovalent alkali metals from the divalent alkaline earth metals. In contrast to such rigid valence-state metals, a core aspect of the fertile chemistry of the actinide (An) 5f-block transition elements is the occurrence of a wide variety of oxidation states, from An^{II} to An^{VII} (and possibly Pu^{VIII}).[1] The highest oxidation states are achieved relatively early in the series, with a maximum stability of the heptavalent state occurring at Np^{VII}. This peak in high oxidation states reflects the decreasing (more negative) energy of the 5f orbitals, and concomitant enhancement in stability of electrons in these orbitals, as the nuclear charge increases beyond Np. The chemical accessibility of the 5f electrons of the early actinides distinctly differs from the relatively inert and localized 4f electrons of the homologous lanthanide (Ln) series, for which the dominant oxidation state is Ln^{III}. Whereas several Ln^{IV}, particularly Ce^{IV}, compounds have been reported,[2,3] only recently was the first Ln^{V} molecule, PrO_2^+, identified.[4] In contrast, the pentavalent oxidation state is known to be stable for several members of the actinide series, beginning with Pa^{V} and continuing through at least Am^{V}. The aqueous actinyl(V) cations, NpO_2^+, PuO_2^+, and AmO_2^+, are particularly important in actinide chemistry.[1] Although aqueous curyl(V) and californyl(V) have been claimed, the evidence for them is dubious; berkelyl(V) has not been reported as a stable species.[1,5,6] There are no claims of oxidation states above An^{III} beyond Cf.

The recent discoveries of Pr^{V} in PrO_2^+ [4] and Ir^{IX} in IrO_4^+ [7] illustrate the ability to create new high oxidation states in isolated gas-phase molecules, particularly in oxide cations. Intrinsically stable high oxidation states can occur in isolated gas-phase molecules because reduction of chemically fragile species by solvents or other interacting moieties is avoided. A central goal of the present work is to evaluate the intrinsic stabilities of the actinyl(V) cations in the gas phase, absent potentially destructive effects in aqueous solution and other condensed phase environments. Gas-phase actinide dioxide cations, AnO_2^+, have been reported for An = Pa,[8] U,[9] Np,[9] Pu,[9] Am,[10], and Cm.[11] Each of these AnO_2^+ ions was produced by the sequential gas-phase reactions of the bare An^+ ions with neutral O-atom donor molecules, to first yield AnO^+ and then AnO_2^+. An aim of the present work is to extend this chemistry further into the actinide series, to BkO_2^+ and CfO_2^+. Although neither berkelyl(V) nor californyl(V) are stable in the condensed phase, it is feasible that they are stable as isolated gas-phase species, in analogy with the PrO_2^+ molecular ion, a moiety that

[a] Dr. P. D. Dau, Dr. J. K. Gibson
Chemical Sciences Division, Lawrence Berkeley National Laboratory
Berkeley, California 94720 (USA)
E-mail: jkgibson@lbl.gov

[b] Dr. M. Vasiliu, Prof. Dr. D. A. Dixon
Department of Chemistry, The University of Alabama
Shelby Hall, Tuscaloosa, Alabama 35487-0336 (USA)
E-mail: dadixon@ua.edu

[c] Prof. Dr. K. A. Peterson
Department of Chemistry, Washington State University
Pullman WA 99164-4630 (USA)
E-mail: kipeters@wsu.edu

Supporting information including ESI mass spectra of the metal ion solutions; NBO6 summary population tables and Mulliken spins at the B3LYP level for $An^{V}O_2^+$, $An^{III}O_2^+$, and $An^{III}O^+$; total energies for linear AnO_2^+, highly bent AnO_2^+, and AnO^+; spin-orbit corrections to the **1**→**2** isomerization energies and the ORCID identification number(s) for the author(s) of this article can be found under https://doi.org/10.1002/chem.201704193.

is not known in condensed phase chemistry. In parallel with the synthesis of new AnO_2^+ molecular ions, electronic structure calculations were performed at the correlated molecular orbital theory coupled cluster CCSD(T) level to assess the structures, including formal actinide oxidation states, for known, new, and predicted AnO_2^+ gas-phase ions for all of the actinides from Pa through Lr. The combined experiment and computational results provide evidence for the synthesis of two new prototypical actinyl(V) molecules, BkO_2^+ and CfO_2^+, and furthermore present an evaluation of the variations in stability of actinyl(V) ions, $[O{=}An{=}O]^+$, across the series and the prospects for producing EsO_2^+ and actinyls of even heavier members of the series. The relative energies of alternative $An^{II}O_2^+$ and $An^{III}O_2^+$ structures having side-on bonded η^2-(O_2) superoxide or peroxide moieties are also assessed.

Results and Discussion

Synthesis of MO_2^+ cations

The ESI mass spectra, obtained with NO_2 in the quadrupole ion trap (QIT), for the five studied metal ions, shown in Figure S1 of the Supporting Information, revealed substantial abundances of MO^+ (M = Ce, Pr, Am, Cf, Bk). The monoxide cation was dominant, except for the case of Bk for which the BkO_2^+ was most abundant. Each of the MO^+ was isolated by ejection of all other ions from the QIT and then exposed to an indeterminate but constant pressure of NO_2 for reaction times ranging from 0.05 to 0.55 s. The results are shown in Figure 1 where it is apparent that each of the five studied monoxide cations abstracted an oxygen atom to yield MO_2^+. The formation of the dioxides occurs by O-atom abstraction from some neutral species RO in the ion trap under thermal conditions: $MO^+ + RO \rightarrow MO_2^+ + R$. As noted below, and expected based on the presence of H_2O in the ion trap,[12,13] hydrolysis of NO_2 yielded HNO_2, as demonstrated by its addition[14] to $PuO(NO_3)_3^-$ to yield $Pu(OH)(NO_2)(NO_3)^-$. It can be inferred that HNO_3 was also produced,[13] and it is known that O_2 is also present in the trap.[12]

The bond dissociation energies (D) for abstraction of an O-atom from the various neutral RO molecules (potentially) present in the ion trap are as follows (in kcal mol^{-1}):[15] D[O-(NO)] = 73.2; D[O-(HNO_2)] = 73.3; D[O-(HNO)] = 101.7; D[O-(H_2)] = 117.3; and D[O-O] = 119.1. Notably, the energies for O-atom abstraction from NO_2 and HNO_3 are essentially the same, which is a manifestation of reaction (1) being nearly thermoneutral.

$$HNO_3 + NO \rightarrow HNO_2 + NO_2 \quad (1)$$

The energies for O-atom abstraction from both NO_2 and HNO_3 are significantly lower, by ≈30 kcal mol^{-1} or more, than those for the other potential O-atom donors in the ion trap. It is hypothesized that the O-atom donor is NO_2, but HNO_3 cannot be excluded as the donor. Because D[O-(NO)] and D[O-(HNO_2)] are essentially the same (73 kcal mol^{-1}), the thermodynamic interpretations of the results are independent of the actual O-atom donor(s).

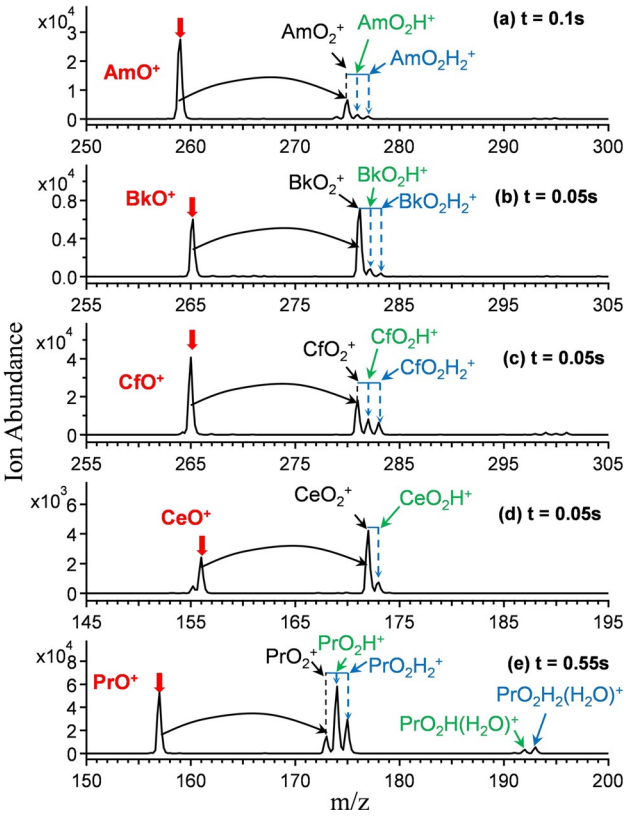

Figure 1. Mass spectra for isolated (a) AmO^+, (b) BkO^+, (c) CfO^+, (d) CeO^+, and (e) PrO^+ after exposure to the same pressure of NO_2 for the indicated time (t). The $^{249}BkO^+$ had decayed to ≈7.6% isobaric $^{249}CfO^+$ at the time of the experiments. H_2O, O_2, and HNO_2/HNO_3 were also present in the ion trap. Water addition to reaction products appears at the longer reaction time for PrO^+.

The results for the reactions of CeO^+ and PrO^+ to yield CeO_2^+ and PrO_2^+ can be compared with previous experimental studies of the gas-phase reactivity of these monoxide cations by Bohme and co-workers.[16,17] It was found that neither CeO^+ nor PrO^+ react with O_2 or H_2O to yield the dioxide cations, [16,17] whereas both react with NO_2 to yield CeO_2^+ and PrO_2^+ according to reaction (2) where M = Ce or Pr.[18]

$$MO^+ + NO_2 \rightarrow MO_2^+ + NO \quad (2)$$

Reaction (2) was reported to occur at 56% of the collisional efficiency for M = Ce but at only 3.7% efficiency for M = Pr. Despite complications introduced by the formation of the hydroxides identified in Figure 1, it is apparent there that CeO_2^+ was similarly produced here with a substantially higher efficiency than PrO_2^+ (note the different reaction times). Schwarz and coworkers also reported reaction (2) for M = Ce, and furthermore found that CeO^+ does not react with N_2O, O_2, or NO.[19] The inability of N_2O, a thermodynamically good O-atom donor (D[O-(N_2)] = 39.9 kcal mol^{-1}), to yield CeO_2^+ suggests that NO_2 distinctively exhibits both the thermodynamic and kinetic attributes necessary to achieve O-atom donation to CeO^+.

Also apparent in Figure 1 are products at 1 and 2 *m/z* higher than the MO_2^+ of primary interest. The $MO_2H_2^+$ products likely

correspond to addition of H_2O to MO^+. These $MO_2H_2^+$ could be physisorption hydrates, $MO(H_2O)^+$, or chemisorption hydroxides, $M(OH)_2^+$, in both of which the oxidation state remains M^{III}. The observed MO_2H^+ are likely hydroxides, $MO(OH)^+$ having oxidation state M^{IV}, possibly produced by (OH)-donation to MO^+ from HNO_2 and/or HNO_3. The values for D[(OH)-(NO)] = 49.2 kcal mol^{-1} and D[(OH)-(NO_2)] = 49.3 kcal mol^{-1} are much lower than D[(OH)-H] = 119.2 kcal mol^{-1};[15] it is known that H_2O is unreactive with both CeO^+ and PrO^+.[17] The origins and nature of the $MO_2H_2^+$ and MO_2H^+, which are likely M^{III} and M^{IV} species, respectively, are not directly pertinent to the synthesis of the MO_2^+ cations that offer the possibility of higher oxidation states.

A detailed description of the structure and energetics of the AnO_2^+ cations is presented below, whereas the computed reactions energetic are described here. We predict the energy for reaction (1) to be nearly thermoneutral at the CCSD(T)/cc-pwCVTZ-DK3/aug-cc-pwCVTZ-DK level of theory at the CCSD(T)/cc-pwCVDZ-DK3/aug-cc-pwCVDZ-DK equilibrium geometries. We also predict the reaction energies for (2) as well as for reactions (3), (4), and (5) as shown in Table 1.

$$HNO_3 + AnO^+ \rightarrow HNO_2 + AnO_2^+ \quad (3)$$

$$AnO^+ + O_2 \rightarrow AnO_2^+ + O \quad (4)$$

$$AnO^+ + HNO_2 \rightarrow AnO_2^+ + HNO \quad (5)$$

Reactions (2) and (3) are exothermic for all An except Cm and Bk; they are nearly thermoneutral for Cf. The endothermic value for reaction (4) for Cm is consistent with the fact that hyperthermal conditions are needed to induce this reaction.[11] Reactions (2) and/or (3) are observed for Bk but we predict them to be endothermic by ≈10 kcal mol^{-1}. This arises because of the aug-cc-pwCVTZ-DK basis set is giving too small bond dissociation energies (i.e., *D*) for the An–O bond in AnO_2^+ (see below). We note that the values for Cf are near thermoneutral, consistent with experiment. The reaction energies are for the formation of the most stable product.

Table 1. Computed reaction energies in kcal mol^{-1}.[a]

	Reaction (2)	Reaction (3)	Reaction (4)	Reaction (5)
Pa	−108.2	−107.0	−63.4	−75.7
U	−95.6	−94.4	−50.8	−63.2
Np	−69.3	−68.1	−24.5	−36.9
Pu	−44.8	−43.6	0.0	−12.3
Am	−14.4	−13.2	30.4	18.1
Cm	12.1 [30.1]	13.3 [31.3]	56.8 [74.9]	44.5 [62.5]
Bk	9.1	10.2	53.8	41.5
Cf	−0.2	0.9	44.5	32.2
Es	−5.5	−4.3	39.3	27.0
Fm	−12.5 [0.5]	−11.3 [1.7]	32.3 [45.2]	19.9 [32.9]
Md	−34.8 [8.2]	−33.7 [9.3]	9.9 [52.9]	-2.4 [40.6]
No	−23.5 [62.5]	−22.3 [63.7]	21.3 [107.3]	8.9 [94.9]
Lr	−11.9 [24.1][b]	−10.7 [25.3][b]	47.3 [83.3][b]	20.5 [56.5][b]
Pr	−30.3	−29.1	14.4	2.1

[a] Values in brackets are for the linear structure **2** (oxidation state V) if it is higher in energy than the highly bent η^2-(O_2) structure **1** in Figure 2. [b] Values in brackets are for the C_{2v} structure of LrO_2^+ with a bond angle of 106.6°. The corresponding values for the linear structure are 28.6, 29.8, 87.8, and 61.0 kcal mol^{-1} in the order of the columns.

Synthesis of dioxide cations including BkO_2^+ and CfO_2^+

It is apparent in Figure 1 that AmO^+ reacts with NO_2 (and/or HNO_3) to yield AmO_2^+, which is presumed to be the linear americyl(V) ion, $[O{=}Am{=}O]^+$, that is well known in condensed phase chemistry.[20] The computational structural and energetic results discussed below support this hypothesis. The AmO_2^+ cation was previously produced by the reaction of AmO^+ with C_2H_4O, ethylene oxide, establishing D[O-(AmO^+)] > D[O-(C_2H_4)] = 84.7 kcal mol^{-1}.[10] The observed reaction of AmO^+ with NO_2 (or HNO_3) is thus thermodynamically favorable. In contrast, oxidation of AmO_2^+ by O_2 or H_2O is not exothermic and is not observed under thermal conditions.[10]

The key results for the reactions of BkO^+ and CfO^+ are shown in Figure 1. They react with NO_2 and/or HNO_3 to yield BkO_2^+ and CfO_2^+. Although absolute reaction efficiencies cannot be derived because the constant pressure of NO_2 is not accurately known, it is apparent from Figure 1 that the reaction efficiency for CfO^+ is somewhat lower than for BkO^+; the reaction efficiency is significantly lower for AmO^+. As noted above, the $^{249}BkO^+$ reactant included ≈7.6% of nearly isobaric $^{249}CfO^+$ when the experiments were performed. The observed different reaction rates and product distributions for BkO^+ versus CfO^+ cannot be attributed to the $^{249}CfO^+$ "impurity" in the former.

The occurrence of reaction (2), or the corresponding reaction (3) with HNO_3 rather than NO_2, establishes a lower limit of D[O-(MO^+)] ≥ 73 kcal mol^{-1} for M = Bk and Cf. Previous attempts to synthesize CmO_2^+ under thermal conditions were unsuccessful.[11] The CmO_2^+ cation was however produced in a hyperthermal reaction of CmO^+ with O_2, demonstrating that CmO_2^+ is an inherently stable species.[11] Based on systematic trends across the actinide series, D[O-(CmO^+)] has been estimated as 48 ± 14 kcal mol^{-1}, a value that is substantially lower than for the earlier AnO_2^+.[21] The authors of that work did not extrapolate these thermodynamic trends beyond CmO_2^+; the present results indicate that D[O-(AnO^+)] does not continue to decrease beyond CmO_2^+ but instead increases for both BkO_2^+ and CfO_2^+. This result is computationally assessed below.

The synthesis of an MO_2^+ cation does not directly reveal its structure or the metal oxidation state. The two plausible geometric structures are shown in Figure 2. In highly bent struc-

Figure 2. Schematic representations of two plausible structures of the MO_2^+ cations. For the η^2-(O_2) highly bent side-on bonded structure **1** the formal oxidation state is M^{II} for a superoxide (O_2^-) and M^{III} for a peroxide (O_2^{2-}). In the "actinyl" structure **2**, which is typically nearly linear, the oxidation state is generally An^V with two double An=O bonds. Exceptions are discussed in the text.

ture **1**, an O_2 moiety is side-on bonded with η^2 coordination. In the case of a superoxide, formally O_2^-, the formal oxidation state is M^{II}, which is the probable situation for a species such as BaO_2^+. In the case of a peroxide, formally O_2^{2-}, the formal oxidation state is M^{III}, which is a stable and feasible oxidation state for all the MO_2^+ synthesized in this work. In structure **2**, which may not be linear as shown in Figure 2, the formal oxidation state ranges from M^{III} for two single M–O$^\bullet$ bonds to M^V for two double M=O bonds; the intermediate M^{IV} oxidation state (or a non-integer oxidation state) would result from bonds of single/double character. It should be noted that structures resulting from other atomic connectivities, specifically M-O-O, are feasible but are almost certainly high-energy (and may not be minima) given the strong binding of O atoms to these metals, and were not studied further computationally.

Previous results for PrO_2^+ indicated structure **2** with a Pr^V oxidation state.[4] The structure of CeO_2^+ was also assigned as **2** but with a formal oxidation state intermediate between Ce^{IV} and Ce^V;[19] a Ce oxidation state above Ce^{IV} is remarkable because it implies chemical engagement of electrons from the closed-shell [Xe] core. The linear AmO_2^+ moiety, structure **2** with Am^V, is common in condensed phase chemistry, and is also likely the structure of the bare cation, as is confirmed below. For the AnO_2^+ beyond AmO_2^+, predicting the structures based on known chemistry is dubious. Consideration of established and estimated reduction potentials[5] suggests that it might be feasible to prepare pentavalent CmO_2^+ and CfO_2^+; unsubstantiated claims have been made for both as unstable solution species.[1] The relatively high reduction potential for Bk^V, and the similar stabilities of Ce^{IV} and Bk^{IV}, suggest the possibility of Bk^{IV} in BkO_2^+. However, the identification of Pr^V in PrO_2^+, an oxidation state that is unknown in the condensed phase, provides a lucid illustration of the limitations of inferring structures and bonding in isolated gas-phase species based on known condensed phase chemistry. Accordingly, high-level electronic structure computations at the coupled cluster CCSD(T) level were employed to assess the nature of the AnO_2^+ molecular ions. The computational results presented below compare favorably with the thermodynamic constraints imposed by the experimental observations.

Computed structures and energetics of AnO_2^+ cations

The key computational results are compiled in Table 2, for the AnO_2^+ from An = Pa through Lr; the first two actinides are not included because their highest practically attainable oxidation states are Ac^{III} and Th^{IV} such that the formation of actinyl(V) species for these two An would require the ionization of inner shell electrons. Both of the types of structures shown in Figure 2 were examined. When the lowest energy structure is **2** for the actinides up to Es, the oxidation state is found to be An^V. For structure **1**, up to Cf, the oxidation state is An^{III}. We base this assignment of oxidation state on the An–O and O–O bond lengths, as well as the electronic population analysis discussed below. The bond length in the prototypical closed shell V species is 1.785 Å for Pa and the bond lengths decrease from Pa to Pu to a minimum value of 1.732 Å for PuO_2^+. The actinyl(V) An–O bond lengths then increase to 1.812 Å for MdO_2^+, with a small decrease at Cf. Thus, the $An^VO_2^+$ from PaO_2^+ through MdO_2^+ exhibit linear structures and An–O bond distances that are characteristic of actinyl(V) ions, with a slight elongation for Md. The bond distance then increases substantially, by 0.05 Å, to 1.870 Å for NoO_2^+; it is thus unlikely that NoO_2^+ is in the V oxidation state, and the actinyl character is apparently disrupted. Because the computed spin on both O atoms is 0.5 we assign the oxidation state as No^{IV}. Notably, the

Table 2. Computed CCSD(T) relative energies (kcal mol^{-1}), geometries and oxidation states (OS) for the linear and bent AnO_2^+.[a]

An	$An^VO_2^+$ f^x (unpaired)	D[O-(AnO^+)][b]	AnO_2^+ Structure **2** r(M-O)[Å][c]	$An^{III}O_2^+$ f^x (unpaired)	AnO_2^+ Structure **1** r(M-O)/r(O-O)[Å]/ OMO[c,d]	$\Delta E/\Delta E+SO$ [Structure **2** → Structure **1**][c]	AnO^+ r(M-O) [Å][f]	Structure **2**/ Structure **1**[c] OS
Pa	0 (0)	178 (186 ± 7)	1.785	2 (2)	2.041/1.539/44.3°	137/135	1.792	V/III
U	1 (1)	166 (177 ± 3)	1.771	3 (3)	2.046/1.544/43.3°	110/110	1.816	V/III
Np	2 (2)	139 (146 ± 3)	1.749	4 (4)	2.038/1.538/43.3°	87/85	1.808	V/III
Pu	3 (3)	115 (122 ± 9)	1.732	5 (5)	2.033/1.519/43.9°	64/69	1.808	V/III
Am	4 (4)	84 (98 ± 13)	1.736	6 (6)	2.036/1.520/43.8°	39/40	1.795	V/III
Cm	5 (5)	58 [40] (48 ± 14)	1.765	7 (7)	2.026/1.562/45.3°	−18/−14	1.819	V/III
Bk	6 (6)	61 (≥73)	1.774	8 (6)	2.012/1.562/45.7°	5/10	1.814	V/III
Cf	7 (5)	70 (≥73)	1.763	9 (5)	2.007/1.543/45.2°	17/23	1.799	V/III
Es	8 (4)	76	1.775	10 (4)	2.229/1.366/35.7°	4/6	1.813	V/II
Fm	9 (3)	82 [70]	1.778	11 (3)	2.223/1.365/35.8°	−13/−3	1.855	V/II
Md	10 (2)	105 [62]	1.812	12 (2)	2.212/1.362/35.9°	−43/−37	1.834	V/II
No	11 (1)	93 [8]	1.870	13 (1)	2.228/1.372/35.9°	−86/−76	1.978	IV/II
Lr	12 (2)	67 [46]	2.048 (1.924)[e]	14 (0)	1.989/1.626/48.2°	−21/−20[e]	1.865	III/III
Pr	0 (0)	100	1.706	2 (2)	2.017/1.529/44.5°	45	1.762	V/III

[a] Relative energies calculated with cc-pwCVTZ-DK3/aug-cc-pwCVTZ-DK basis sets at CCSD(T)/cc-pwCVDZ-DK3/aug-cc-pwCVDZ-DK equilibrium geometries. [b] Values in parentheses from experiment, Ref. [21]. Values in brackets for the V linear OS; IV for No and III for Lr. [c] See Figure 2 for structures. ΔE = electronic energy difference with a positive value meaning that Structure 2 is more stable. $\Delta E+SO=\Delta E$ + spin orbit correction. See the text. [d] R(O–O): O_2^- ($^2\Pi_g$) = 1.365 Å, O_2^{2-} ($^1\Sigma_g^+$) = 1.631 Å, in H_2O_2 = 1.478 Å. [e] LrO_2^+ ground-state is best described as "non-actinyl" (OMO 106.6°), linear singlet for LrO_2^+ (in parenthesis) is 4.5 kcal mol^{-1} above the bent actinyl structure. [f] AnO^+ OS is III for all except No, which is assigned II.

stability of this $No^{IV}O_2^+$ "actinyl" is much lower, by 86 kcal mol^{-1}, than the η^2 $No^{II}O_2^+$ structure. LrO_2^+ has a much longer bond length, 2.05 Å, and is bent with a bond angle of 107°. The corresponding linear structure for LrO_2^+ is only 4.5 kcal mol^{-1} higher in energy. Thus it is probably best to describe ground-state highly bent η^2 LrO_2^+ as a Lr^{III} peroxide and the higher-energy less bent structure as a non-actinyl, also having the oxidation state III with a closed shell Lr and two O atoms with an open-shell electron on each.

The dominant electronic configurations of the linear AnO_2^+ are given in Table 3 as determined in the current work. Denning[22] has given a description of the orbital ordering in the actinyls built on experimental data for the earlier actinyls. The

Table 3. Electronic states for linear AnO_2^+

An^V	# 5f electrons	Ground Term	f orbital occupation
Pa	0	$^1\Sigma_g^+$	
U	1	$^2\Phi_u$	ϕ^1
Np	2	^3H_g	$\phi^1\delta^1$
Pu	3	$^4\Phi_u$	$\phi^1\delta^2$
Am	4	$^5\Sigma_g^+$	$\phi^2\delta^2$
Cm	5	$^6\Pi_u$	$\phi^2\delta^2\pi^1$
Bk	6	$^7\Sigma_g^-$	$\phi^2\delta^2\pi^2$
Cf	7	$^6\Delta_u$	$\phi^2\delta^3\pi^2$
Es	8	$^5\Gamma_g$	$\phi^3\delta^3\pi^2$
Fm	9	$^4\Phi_u$	$\phi^3\delta^4\pi^2$
Md	10	$^3\Sigma_g^-$	$\phi^4\delta^4\pi^2$
No	11	$^2\Pi_u$	$\phi^4\delta^4\pi^3$
Lr	12	$^1\Sigma_g^+$	$\phi^4\delta^4\pi^4$

two lowest lying orbitals for the f electrons are the $1\delta_u$ and the $1\varphi_u$, which are very close in energy and have no contribution from the oxygen 2p orbitals. These are followed energetically by the $3\pi_u$* and then by the $4\sigma_u$*, both of which contain some contribution from the O electrons. Electronic structure CASSCF/CASPT2 calculations[23] have been reported for PaO_2^+ to CmO_2^+ and the results are in agreement with our values in Table 3. The f electrons want to remain high spin so the $1\delta_u$ and the $1\varphi_u$ take the first 4f electrons. At Cm, the $3\pi_u$* becomes occupied and a second f electron is added to the $3\pi_u$* for Bk. Rather than occupying the $4\sigma_u$* and staying high spin, the f electrons go back to filling the $1\delta_u$ and the $1\varphi_u$ with 2 electrons in the $3\pi_u$* for Cf to Md. For No and Lr, the f electrons are added to the $3\pi_u$*. We note that filling the $3\pi_u$* leads to a change in the oxidation state and No and Lr are no longer in the V oxidation state for the AnO_2^+. Notably "actinyl" NoO_2^+ is linear whereas LrO_2^+ is bent to 107° with the linear structure 4.5 kcal mol^{-1} higher in energy. The prior work[23] on linear AnO_2^+ up to An=Cm showed that the these ions are dominated by a single configuration with at least the wavefunction being dominated by >80% of a single configuration. In fact, all of the $AnO_2^{0/+/2+}$ were shown to be dominated by a single configuration in the CASPT2 calculations for Pa to Cm.

The η^2-structure is very bent with a bond angle up through Cf of 43–46° and an O–O bond distance of 1.52 to 1.56 Å, which is very similar to the O_2^{2-} distance of 1.63 Å at this level of theory. The An–O bond distance is much longer, 2.01 to 2.05 Å. Thus, in this case, the An is clearly in the III oxidation state. For Es to No, the η^2-structure is more like a superoxide with a smaller bond angle near 36°, a shorter O–O bond of 1.36–1.37 Å comparable to that of O_2^- (1.365 Å), and a very long An–O bond of 2.21 to 2.23 Å. These structures are best described as being in the II oxidation state. For LrO_2^+, the strongly bent structure is again in the III oxidation state, with a larger O–O bond and a larger angle to accommodate the O_2^{2-}. Due to the low symmetry, there is substantial mixing of the orbitals on the An and it is not possible to make a simple assignment of the electronic configuration as for the linear structure.

The bond distances show that there is a crossover from the III to the II oxidation state for the η^2-structures as the O_2 goes from a peroxide (O_2^{2-}) to a superoxide (O_2^-). This occurs between Cf and Es with a reversion back to III at Lr. It is clear that the II formal oxidation state occurs for the bent structure of Es as one of the open-shell electrons switches from a 5f δ as found for Cf to an O $2p_x$ for Es. The only real change in the linear actinyl-type structures is for No and Lr where the Lr is in the III oxidation state and the No is assigned as IV based on the spin 0.5 on both O atoms.

How do the relative energetics of the two structures change as one goes across the actinide row? The comparative energies of the $An^VO_2^+$ and $An^{III}O_2^+$ (or $An^{II}O_2^+$), along with the [O-(AnO^+)] dissociation energies, are given in Table 2 and plotted in Figure 3. For Pa to Am, the η^2-structure with the An in the III oxidation state is much higher in energy than the linear V oxi-

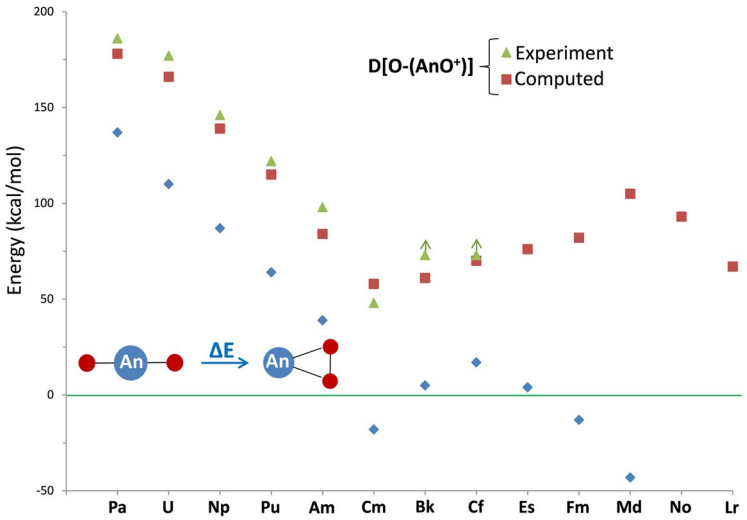

Figure 3. Plot of bond dissociation energies D[O-(AnO^+)] from Table 2. The red squares are the computed energies; the green triangles are the available experimental values, which are lower limits from this work for BkO_2^+ and CfO_2^+. The blue diamonds are energies for converting the actinyl(V) ions to the η^2-(O_2) structure. For AnO_2^+ having conversion energies below zero the η^2-(O_2) structure **1** is more stable than the actinyl structure **2**. Conversion energies are not included for NoO_2^+ and LrO_2^+ because they do not exhibit actinyl(V) structures.

dation state structure. At Cm, the energy difference switches so that the III η^2-structure is favored because the III oxidation state has the quite stable $5f^7$ electron configuration, whereas the V oxidation state has 5 unpaired electrons. The energy difference between the two AnO_2^+ isomers is very small for Bk with the linear V only favored by 10 kcal mol^{-1}. The linear V structure for Cf is stable by 23 kcal mol^{-1} as compared to the III η^2-structure. The V structure for Es is only 6 kcal mol^{-1} more stable than the II η^2-structure. A crossover occurs between Es and Fm, and the lowest energy structure for Fm is predicted to be the η^2-structure. The η^2-structure becomes more stable as one continues across the row to No. At Lr, the η^2-structure is still the most stable, but the energy difference has significantly decreased from that for No.

The maximum effect of spin orbit interactions for the energy difference between the two structures is <10 kcal mol^{-1}. Except for Pa and Np, the spin orbit effects are always positive for the energy difference as written. This leads to an increase in the positive energy differences and will lead to a less negative value for the negative energy differences. None of the signs change when the effect of spin orbit is included. The effect for Cm is to change the energy difference from -18 to -14 kcal mol^{-1}, for Bk, it increases the energy difference from 5 to 10 kcal mol^{-1}, and for Es, it increases the energy difference from 4 to 6 kcal mol^{-1}. The largest effect is to change the energy difference for Fm from -13 to -3 kcal mol^{-1}. Except for Es and Fm, it is unlikely that higher level multi-reference configuration interaction calculations and spin orbit calculations will impact the sign of the energy difference between structure **1** and structure **2**.

The computational results for PrO_2^+ are included in Table 2. The results confirm the previous report that PrO_2^+ is linear "praseodymyl(V)".[4] The stability of $Pr^VO_2^+$ is comparable to that of $Am^VO_2^+$, as indicated by both their similar bond dissociation energies and their energies relative to the trivalent peroxides. The experimental results establish a lower limit for D[O-(PrO^+)] of 73 kcal mol^{-1}, revealing a remarkably high stability of this Pr^V molecule.

The value for D[O-(AnO^+)] is the energy for reaction (6) where the oxidation states are designated as X and Y for the dioxo and monoxo cations, respectively. The oxidation states X were discussed above, those for the monoxides, that is, Y, are considered here.

$$An(X)O_2^+ \rightarrow An(Y)O^+ + O \qquad \Delta E = D[O\text{-}(AnO^+)] \qquad (6)$$

We note that the computed An–O bond distances for the AnO^+ fall within the range of 1.79 to 1.86 Å except for No, where the bond distance is much longer at 1.98 Å (Table 1). We can thus assign the An oxidation state Y in reaction (6) as III in AnO^+ for all of the An except for No, where it is better assigned as II. The computed values for D[O-(AnO^+)] are given in Table 2 together with estimates based on experimental results; the computed values are plotted in Figure 3. The agreement between the experimental and computed values is very good, and both indicate a monotonic decrease in bond dissociation energy from PaO_2^+ to CmO_2^+. We note that the value for linear CmO_2^+ is quite low, 40 kcal mol^{-1}, consistent with a high spin f^7 occupation for the III oxidation state in CmO^+ that increases the stability of the monoxide. The actual bond energy for the most stable CmO_2^+ is 58 kcal mol^{-1} for the η^2-structure with Cm^{III}. A simplistic extrapolation of this trend for the linear AnO_2^+ would predict even lower D[O-(AnO^+)] for An = Bk and Cf, whereas the computational results in Table 2 indicate that the dissociation energy for BkO_2^+ is about 21 kcal mol^{-1} higher than the value for linear CmO_2^+. The value for Cf is about 30 kcal mol^{-1} higher in energy and that for Es is about 36 kcal mol^{-1} higher, both with respect to linear CmO_2^+. The validity of the computed D[O-(BkO^+)] and D[O-(CfO^+)], 61 and 70 kcal mol^{-1}, respectively, is bolstered by the new experimental lower limit of 73 kcal mol^{-1} for both. Although the computed values are below the new experimental lower limit, the CCSD(T) values with this basis set are found to be somewhat low as compared to experiment as evidenced by the comparison between theory and experiment for the earlier AnO_2^+ species in Table 2.

The D[O-(AnO^+)] starting at FmO_2^+ (and for CmO_2^+) are for the η^2-structures. The value for η^2-FmO_2^+ is comparable to that for linear AmO_2^+ and that for η^2-MdO_2^+ is comparable to that for PuO_2^+. The D[O-(AnO^+)] then decrease for η^2-NoO_2^+ and η^2-LrO_2^+ with the value for LrO_2^+ similar to those for BkO_2^+ to EsO_2^+. The D[O-(AnO^+)] for the linear isomer for the later actinides decrease from Fm to No, where a small value of 8 kcal mol^{-1} is predicted, and then increases to 46 kcal mol^{-1} for Lr. The D[O-(PrO^+)] falls between those of AmO_2^+ and PuO_2^+, consistent with the above discussion.

Up to Es, excluding Cm, reaction (6) corresponds to reduction of An^V to An^{III}, so one can correlate the trends in bond dissociation energies with estimated reduction potentials E^0.[5] The E^0[IV/III] are similarly high ($\approx$3.1 V) for Cm and Cf, neither of which exhibit particularly stable An^{IV} oxidation states in the condensed phase. E^0[IV/III] for Bk is much lower, 1.67 V, and Bk^{IV} is stable in solutions and solids. The E^0[V/IV] for Cf is only $\approx$1.0 V, which reflects the stability of the half-filled $5f^7$ valence orbital shell in Cf^V. In contrast, E^0[V/IV] for Cm is $\approx$1.6 V, and E^0[V/IV] for Bk is much higher at $\approx$3.1 V. Based on the (estimated) reduction potentials, it is expected that Cf^V should be more stable than Cm^V. This is in line with what has been predicted, and the favored oxidation state for CmO_2^+ is actually III with the η^2-structure.

A particularly remarkable result is that Bk^V is comparably stable to Cf^V, with the predicted relatively high stability of the latter expected due to its $5f^7$ configuration. Based on the solution reduction potentials, it is expected that Bk^V should be much more susceptible towards reduction to Bk^{IV}, though not towards further reduction to Bk^{III}. The latter prediction is in accord with the higher stability of $Bk^VO_2^+$ versus $Bk^{III}O_2^+$. The result that the oxidation state is Bk^V rather than Bk^{IV} in BkO_2^+ is a manifestation of the very different chemistry in the gas phase versus solution and solid. E^0[V/IV] reflects the (free) energy for reduction of BkO_2^+(aq) to Bk^{4+}(aq), which is clearly a very different process from conversion of $Bk^VO_2^+$(g) to $Bk^{IV}O_2^+$(g). The results here indicate that it is more favorable for the BkO_2^+ cation to have two Bk=O double bonds rather than intermediate bond orders to yield Bk^{IV}. Solution reduction

entirely excludes from consideration the non-ionic character of the bonding in BkO_2^+, and specifically significant bond covalency.[24] In this regard, it should be emphasized that the synthesis of the $Bk^{V}O_2^+$ molecular ion does not suggest that aqueous berkelyl(V) is expected to be a stable solution species. Similarly, neither "praseodymyl(V)" nor Ir^{IX} are likely to be stable in condensed phase; substantial effort was made to produce the latter but to no avail.[7] The AnO_2^+ oxidation states assigned here are shown in Table 4 along with the known (and proposed) actinide oxidation states.[25–31]

Table 4. Previously reported An oxidation states and those identified here for molecular AnO_2^+.[a]

Ac	Th	Pa	U	Np	Pu	Am	Cm	Bk	Cf	Es	Fm	Md	No	Lr
	2		2	2	2	2			2	2	2		**2**	
										2	***2***	***2***	***2***	
3	3	3	3	3	3	**3**	**3**	**3**	**3**	**3**	**3**	**3**	3	**3**
			3	*3*	*3*	*3*	***3***	*3*	*3*					***3***,3
	4	4	4	4	**4**	4	4	4	4	4?			4	
		5	5	**5**	5	5	5?		5?					
		5	**5**	**5**	**5**	**5**	**5**	**5**	**5**	**5**	**5**	**5**		
			6	6	6	6	6?							
				7	7	7?								
					8?									

[a] States with question marks are unsubstantiated. The most stable OS is in bold (see text for references). The computed AnO_2^+ OS are in red. The ground state is in bold. Underlined values correspond to $[O{=}An{=}O]^+$ actinyls. Italicized values correspond to highly bent η^2-(O_2) An^{III} peroxides or An^{II} superoxides.

Natural population analysis (NPA)

The Natural Population Analysis based on the Natural Bond Orbitals (NBOs)[32,33] using NBO6[34,35] was performed with densities and Kohn–Sham orbitals calculated with the B3LYP functional and the basis sets given above using Gaussian 09. The charges are given in the Supporting Information. For the $An^{V}O_2^+$ actinyl type structures, the An charges range from +1.88 (Md) to +2.31 (U). Except for Md, most of the values fall in the range of +2.10 to +2.31 with Am being the other outlier at +2.00. For Pa, there are 1.85 e in the 5f and ≈0.9 e in the 6d. These are in doubly occupied orbitals and are due to backbonding from the O atoms to the An. Proceeding from U to Fm, the 6d orbitals are approximately doubly occupied (backbonding) and have a population of 0.75 to 0.9 e. The doubly occupied 6d orbitals are not important for the determination of the electronic states given in Table 3 which arise from how the 5f orbitals are occupied. Except for Lr, the 7s occupancy is very small. For $^2UO_2^+$, there is one unpaired 5f electron and two paired 5f electrons representing backbonding from the O. There is only a small spin polarization on the O atoms. The two 5f electrons involved in backbonding persist through Cm and there is an increase in the spin polarization with ≈0.25 e excess β electron spin on each O. At Bk, there is no longer any negative spin polarization and there is ≈0.25 e of α spin on each O. For Cf, which is a sextet, there is ≈0.25 e of α spin on each O and there are 4.5 paired 5f electrons showing an increase in the backbonding or additional pairing on the Cf. From Bk to Lr, excluding Md, there are ≈6.8 to 7 e α electrons on the An in the 5f and the amount of spin pairing increases. In addition, the excess α spin on O increases as well. We note that the crossover from the An^{V} actinyl to the An^{III} η^2-structure occurs between Es and Fm in terms of the energetics. For Md, the electronic structure dramatically changes with significant α spin on each O (1.4 e) and a large β spin on the Md for the 5f electrons. The charge on the Md is clearly decreased and the 6d population (mostly doubly occupied) is also decreased to <0.2 e.

For the $An^{III}O_2^+$ η^2-structures, there is a charge of ≈ +2.1 on the An for Pa to Bk excluding Am, which is ≈ +1.9. The charges for Es to No are ≈ +1.8 and this increases to +2.2 for Lr. Except for Am, there is very little spin on the O up to Bk. For Am, there is a substantial β spin of −0.27 e on the O. From Es to Lr, there is about 0.5 e α spin on each O, consistent with an O_2^- species. For Pa to Cm, there is very little backbonding in the 5f in terms of the amount of β spin except for Am where there is 1.1 e of β spin. There is always excess α spin in the 6d orbitals with only about 0.5 e spin paired backbonding and the 6d population decreases from Pa to a low value of 0.40 e for Am. It then increases to Cm with small decreases to Bk and Cf. At Es, the 6d population is only ≈0. 2 e and is essentially all spin paired due to backbonding. Except for Pa and Lr at the ends of the period, there is very little 7s character. For Bk and Cf, there are 2.7 and 2.8 spin paired 5f electrons and then the number of spin paired 5f electrons is 8, 10, 12, and 14 for Es, Fm, Md, No, and Lr, respectively.

The energy differences between the $An^{V}O_2^+$ actinyl and $An^{III}O_2^+$ η^2-structures are less than ±20 kcal mol^{-1} for Cm to Fm. It is in this region that spin pairing of the 5f β electrons begins to occur and there is a slight decrease in the 6d population from Bk to Fm for $An^{V}O_2^+$. For $Cm^{III}O_2^+$, the amount of backbonding into the 5f is sufficiently small that Cm can attain a $5f^7$ configuration and the η^2-structure is more stable than the actinyl, as noted above. For the $An^{III}O_2^+$ from Bk to Fm, there are always 7 5f electrons with α spin and spin pairing of the 5f electrons begins to occur. For $Bk^{III}O_2^+$ and $Cf^{III}O_2^+$, there is 0.2 to 0.3 e excess α spin on the O atoms so there is some spin polarization on the An. At Es, the η^2-structure changes to O_2^- from O_2^{2-} for $An^{III}O_2^+$ and the energy differences between the actinyl and peroxy structures are small. For Es, the actinyl is slightly favored and for Fm, the η^2-structure is favored. For Es and Fm, there is very little backbonding into the 6d for $An^{III}O_2^+$ η^2-structure in contrast to the actinyl structures where significant 6d backbonding is still present.

The $An^{III}O^+$ have small amounts of spin polarization on the O up to Cm and the amounts are very similar to the values for the $An^{III}O_2^+$ η^2-structure. The values of the α spin on the O increase from 0.03 e for Cm to 1.00 e for No. Except for No and Lr, there are essentially no contributions from the 7s electrons. The amount of 6d orbital participation decreases from 1.12 e for Pa to 0.16 e for No and then increases to 0.66 e for Lr. There is always excess α spin in the 6d with approximately 0.5 to 0.6 e spin paired on the An up to Es; this excess spin decreases to 0.16 e for No. Up to Cm, there is only a modest

amount of spin pairing for the 5f on the An of 0.4 to 0.6 e due to backbonding. For Cm to Lr, there are approximately 7 5f α electrons and the 5f electrons pair up. Due to the positive spin on O for the heavier actinides, there is always somewhat less spin than expected on the An.

Summary and Conclusions

The two new actinide dioxide molecular ions, BkO_2^+ and CfO_2^+, were synthesized in the gas phase by oxygen atom transfer from NO_2 (or HNO_3) to BkO^+ and CfO^+ under thermal conditions ($\approx$300 K) in an ion trap. The AnO_2^+ molecular ion had previously been synthesized for An = Pa through Cm; the experimental (or estimated) dissociation energies, D[O-(AnO^+)], monotonically decrease from Pa to Cm such that it was anticipated that AnO_2^+ beyond CmO_2^+ would be decreasingly stable and synthetically inaccessible. However, CCSD(T) computations predict an increase in D[O-(AnO^+)] beyond CmO_2^+; these values, plotted in Figure 3, follow the same trend as the experimental values but are generally lower by $\approx$10 kcal mol^{-1}. The observed, but not empirically expected, syntheses of BkO_2^+ and CfO_2^+ are thus consistent with computations and provide substantiation of theory, which is further validated by the result here that PrO_2^+ is a lanthanide(V) species. The computed lowest-energy structures of the two new AnO_2^+ molecules are linear pentavalent actinyls, $[O{=}An{=}O]^+$, with the energies of alternative structures too low to be synthesized by the employed approach. The actinyl(V) series has thus been extended to "berkelyl" and "californyl", these being the first Bk^V and Cf^V species.

The CCSD(T) computations were extended to all AnO_2^+ from PaO_2^+ through LrO_2^+. The D[O-(AnO^+)] are sufficiently high (>50 kcal mol^{-1}) that all of these AnO_2^+ should be synthetically accessible by oxygen atom transfer to the corresponding AnO^+. The two viable considered structures of the AnO_2^+ are: linear, or sufficiently close to linear, such that there is no O–O bonding interaction, referred to as actinyl-like; and highly bent with a side-on bonded $\eta^2(O_2)$ moiety that may be either a superoxide (O_2^-) or peroxide (O_2^{2-}). For PaO_2^+ through AmO_2^+, linear actinyl structures with two short An=O bonds are clearly the most stable. In contrast, the lowest energy structure of CmO_2^+ is a highly bent peroxide η^2-structure in which the oxidation state is $5f^7$ Cm^{III}. For BkO_2^+ and CfO_2^+ the actinyl(V) structures are somewhat more stable than the An^{III} peroxides, and for EsO_2^+ the Es^V structure is slightly more stable than the Es^{II} superoxide. Beginning with FmO_2^+ the An^{II} superoxides become more stable, with the trivalent peroxide the most stable in the case of Lr due to the stability of closed-shell $5f^{14}$ Lr^{III}.

In addition to the first synthesis of Bk^V and Cf^V molecules, a particularly significant result of this work is the revelation that the AnO_2^+ actinyl(V) structure are the most stable dioxide cations for all of the An from Pa through Es (except Cm), and that the linear actinyl(V) ions are local energy minima through MdO_2^+. These results expand the knowledge of actinide oxidation states to Bk^V and Cf^V and extend the distinctive actinyl motif towards the end of the series.

Methods

Experimental Section

Caution: The ^{242}Pu, ^{243}Am, ^{249}Bk, and ^{249}Cf employed in these experiments are highly radioactive isotopes that can be safely handled only using rigorous radiological control procedures in an approved facility.

The following stock solutions were used to prepare electrospray ionization (ESI) solutions: $^{243}AmO_2(NO_3)_3^-$ at pH 1; 10 mM $CeBr_3$ in water; 10 mM $PrBr_3$ in water. For Cf, a solution of 0.40 mM ^{249}Cf in 100 mM HCl was slowly evaporated to yield a solid californium chloride that was dissolved to produce the ESI solution. The ^{249}Bk supplied by Oak Ridge National Laboratory as solid $BkCl_3$ was dissolved to a concentration of 10 mM in ethanol/water. At the time of the experiments the ^{249}Bk, which has a 320 day half-life, had partially beta-decayed to yield $\approx$7.6% of progeny ^{249}Cf impurity, which is practically isobaric and indistinguishable except by high-resolution mass spectrometry. For all the metals, dilution yielded an ESI solution of $\approx$100 μM metal ion in $\approx$80% ethanol and $\approx$20% water. A ^{242}Pu nitrate solution was prepared as described previously to monitor the presence of HNO_2 in the quadrupole ion trap mass spectrometer (QIT/MS).[14]

The ESI mass spectrometry experiments were performed using an Agilent 6340 QIT/MS. The containment of the ESI source in a radiological glove box enables handling of highly radioactive isotopes such as ^{242}Pu, ^{243}Am, ^{249}Bk and ^{249}Cf.[36] Additionally, ions in the trap can undergo ion-molecule reactions for a fixed time at $\approx$300 K.[37] In high resolution mode, the instrument has a detection range of 50–2200 *m/z* and a resolution M/ΔM of $\approx$3000. Mass spectra were acquired using the following instrumental parameters: solution flow rate, 60 μl min^{-1}; nebulizer gas pressure, 12 psi; capillary voltage and current, 4350 V, 50.0 nA; end plate voltage offset and current, −500 V, 275 nA; dry gas flow rate, 3 l min^{-1}; dry gas temperature, 325 °C; capillary exit, 300.0 V; skimmer, 40.5 V; octopole 1 and 2 DC, 16.5 V and 0.0 V; octopole RF amplitude, 104 V_{pp}; lens 1 and 2, −100.0 V and −10.5 V; trap drive, 52. The parameters for the $PuO(NO_3)_3^-$ calibration experiments were described previously.[14] High-purity nitrogen gas for nebulization and drying in the ion transfer capillary was supplied from the boil-off of a liquid nitrogen Dewar. The helium buffer gas pressure in the trap is constant at $\approx10^{-4}$ torr.

The ion trap has been modified to allow for the introduction of reagent gases, NO_2 (≥99.5%, Sigma Aldrich) for the present study, through a vacuum manifold a leak valve.[36] The NO_2 pressure was not known but was essentially constant for all of the experiments. As has been discussed elsewhere, the background water pressure in the ion trap is estimated as $\approx10^{-6}$ torr; reproducibility of hydration rates of $UO_2(OH)^+$ confirms that the background water pressure in the trap varies by less than ±10%.[12] A manifestation of the presence of water in the trap is surface-catalyzed hydrolysis of NO_2 to yield HNO_2 and HNO_3.[13] The presence of HNO_2 was confirmed by its addition to $PuO(NO_3)_3^-$, produced as described previously,[14] to yield $Pu(OH)(NO_2)(NO_3)_3^-$. Although the presence of HNO_3 was not similarly demonstrated by the appearance of $Pu(OH)(NO_3)_4^-$, this negative result does not exclude HNO_3 as a possible reactant gas in the ion trap.

Computational

The geometries were initially optimized and vibrational frequencies were calculated at the density functional theory (DFT)[38] level with

the hybrid B3LYP exchange correlation functional.[39,40] The aug-cc-pVDZ basis set[41,42] was used for O and the aug-cc-pVDZ-PP basis sets[43–46] with effective core potentials were used for An = U and Pa, and the Stuttgart large core effective core potential[47] and associated basis sets[48,49] for the remaining An. The DFT calculations provided starting geometries for subsequent CCSD(T) calculations. The DFT calculations were done with the Gaussian 09 program system.[50]

Starting from the DFT optimized geometries, CCSD(T)[51–54] (coupled cluster theory with single and double excitations and a perturbative triples correction) geometry optimizations using the 3rd-order Douglas–Kroll–Hess Hamiltonian[55–57] were carried out using the aug-cc-pwCVDZ-DK for O[42,58,59] and cc-pwCVDZ-DK3 for An[43,60] basis sets. This is denoted in the text as CCSD(T)/cc-pwCVDZ-DK3/aug-cc-pwCVDZ-DK. Single-point CCSD(T) calculations were then carried out at these geometries using the analogous TZ basis sets. The calculations did not correlate the electrons up through $n=4$ on the actinide (60 electrons in the core) and correlated the remaining actinide electrons and all of the electrons on O. The open-shell calculations were done with the R/UCCSD(T) approach where a restricted open shell Hartree–Fock (ROHF) calculation was initially performed and the spin constraint was then relaxed in the coupled cluster calculation.[53,61–63] Only the geometries were optimized at the CCSD(T) level. The CCSD(T) method with the chosen basis set combination was chosen as a compromise between reliable predictions and computational efficiency. As noted above, the available multi-reference calculations[23] show that the electronic state of the AnO_2^+ is dominated by a single reference so the CCSD(T) method is an acceptable computational approach. Because of the change in electron configurations between the "linear" and highly bent structures, a very large multi-reference calculation would be required including the actinide 5f electrons and the O 2p electrons in an orbital space including the An 5f and 6d and O 2p orbitals. The CCSD(T) calculations were performed with the MOLPRO 2012 program package.[64,65] The spin-orbit calculations were performed with the ADF code[66,67] at the ZORA-spin orbit level[68–72] with the BLYP functional[40,73] and the TZ2P basis set. The calculations were performed on our local (UA and WSU) Opteron-based and Xeon-based Linux clusters.

Acknowledgements

The work of P.D.D. and J.K.G. was supported by the U.S. Department of Energy, Office of Basic Energy Sciences, Heavy Element Chemistry program (U.S. DOE, OBES, HEC) at LBNL under Contract No. DE-AC02-05CH11231. D.A.D. acknowledges the support of U.S. DOE, OBES, Geochemistry program, through a subcontract from the Pacific Northwest National Laboratory. D.A.D. thanks the Robert Ramsay Fund at the University of Alabama. K.A.P. acknowledges the support of the U.S. DOE, OBES, HEC through Grant No. DE-FG02-12ER16329. The isotopes used in this research were supplied by the U.S. Department of Energy, Office of Science, by the Isotope Program in the Office of Nuclear Physics. The ^{249}Bk was provided to LBNL through the Isotope Development and Production for Research and Applications Program through the Radiochemical Engineering and Development Center at Oak Ridge National Laboratory.

Conflict of interest

The authors declare no conflict of interest.

Keywords: actinides · density functional calculations · gas-phase reactions · redox chemistry · transuranium elements

[1] *Summary and Comparison of Properties of the Actinide and Transactinide Elements in The Chemistry of the Actinide and Transactinide Elements, Vol. 3*, 3rd ed. (Eds.: L. R. Morss, N. M. Edelstein, J. Fuger), Springer, Dordrecht, **2006**, pp. 1753 – 1835.
[2] N. A. Piro, J. R. Robinson, P. J. Walsh, E. J. Schelter, *Coord. Chem. Rev.* **2014**, *260*, 21 – 36.
[3] T. Vent-Schmidt, Z. Fang, Z. Lee, D. A. Dixon, S. Riedel, *Chem. Eur. J.* **2016**, *22*, 2406 – 2416.
[4] Q. N. Zhang, S. X. Hu, H. Qu, J. Su, G. J. Wang, J. B. Lu, M. H. Chen, M. F. Zhou, J. Li, *Angew. Chem. Int. Ed.* **2016**, *55*, 6896 – 6900; *Angew. Chem.* **2016**, *128*, 7010 – 7014.
[5] F. David, *J. Less-Common Met.* **1986**, *121*, 27 – 42.
[6] V. N. Kosyakov, E. A. Erin, V. M. Vityutnev, V. V. Kopytov, A. G. Rykov, *Soviet Radiochem.* **1982**, *24*, 455 – 457.
[7] G. J. Wang, M. F. Zhou, J. T. Goettel, G. J. Schrobilgen, J. Su, J. Li, T. Schloder, S. Riedel, *Nature* **2014**, *514*, 475 – 477.
[8] M. Santos, A. Pires de Matos, J. Marçalo, J. K. Gibson, R. G. Haire, R. Tyagi, R. M. Pitzer, *J. Phys. Chem. A* **2006**, *110*, 5751 – 5759.
[9] M. Santos, J. Marçalo, A. Pires de Matos, J. K. Gibson, R. G. Haire, *J. Phys. Chem. A* **2002**, *106*, 7190 – 7194.
[10] M. Santos, J. Marçalo, J. P. Leal, A. Pires de Matos, J. K. Gibson, R. G. Haire, *Int. J. Mass Spectrom.* **2003**, *228*, 457 – 465.
[11] J. K. Gibson, R. G. Haire, M. Santos, A. Pires de Matos, J. Marçalo, *J. Phys. Chem. A* **2008**, *112*, 11373 – 11381.
[12] D. Rios, M. C. Michelini, A. F. Lucena, J. Marçalo, T. H. Bray, J. K. Gibson, *Inorg. Chem.* **2012**, *51*, 6603 – 6614.
[13] B. J. Finlayson-Pitts, L. M. Wingen, A. L. Sumner, D. Syomin, K. A. Ramazan, *Phys. Chem. Chem. Phys.* **2003**, *5*, 223 – 242.
[14] R. Maurice, E. Renault, Y. Gong, P. X. Rutkowski, J. K. Gibson, *Inorg. Chem.* **2015**, *54*, 2367 – 2373.
[15] *NIST Chemistry WebBook*, NIST Standard Reference Database Number 69. (Ed.: P. J. Linstrom), U.S. Department of Commerce, Washington, **2016**, Vol. **2017**.
[16] G. K. Koyanagi, D. K. Bohme, *J. Phys. Chem. A* **2001**, *105*, 8964 – 8968.
[17] P. Cheng, G. K. Koyanagi, D. K. Bohme, *ChemPhysChem* **2006**, *7*, 1813 – 1819.
[18] M. J. Y. Jarvis, V. Blagojevic, G. K. Koyanagi, D. K. Bohme, *Phys. Chem. Chem. Phys.* **2010**, *12*, 4852 – 4862.
[19] C. Heinemann, H. H. Cornehl, D. Schroder, M. Dolg, H. Schwarz, *Inorg. Chem.* **1996**, *35*, 2463 – 2475.
[20] W. H. Runde, B. J. Mincher, *Chem. Rev.* **2011**, *111*, 5723 – 5741.
[21] J. Marçalo, J. K. Gibson, *J. Phys. Chem. A* **2009**, *113*, 12599 – 12606.
[22] R. G. Denning, *J. Phys. Chem. A* **2007**, *111*, 4125 – 4143.
[23] I. Infante, A. Kovacs, G. La Macchia, A. R. M. Shahi, J. K. Gibson, L. Gagliardi, *J. Phys. Chem. A* **2010**, *114*, 6007 – 6015.
[24] N. Kaltsoyannis, *Dalton Trans.* **2016**, *45*, 3158 – 3162.
[25] N. Kaltysoyannis, P. Scott, *The f elements*, Oxford University Press, Oxford, **2007**.
[26] S. Cotton, *Lanthanide and Actinide Chemistry*, Wiley, Hoboken, **2007**.
[27] C. J. Windorff, P. Chen, J. N. Cross, W. J. Evans, F. Furche, A. J. Gaunt, M. T. Janicke, S. A. Kozimor, B. L. Scott, *J. Am. Chem. Soc.* **2017**, *139*, 3970 – 3973.
[28] C. J. Windorff, M. R. MacDonald, K. R. Meihaus, J. W. Ziller, J. R. Long, W. J. Evans, *Chem. Eur. J.* **2016**, *22*, 772 – 778.
[29] R. R. Langeslay, G. P. Chen, C. J. Windorff, A. K. Chan, J. W. Ziller, F. Furche, W. J. Evans, *J. Am. Chem. Soc.* **2017**, *139*, 3387 – 3398.
[30] W. J. Evans, *Organometallics* **2016**, *35*, 3088 – 3100.
[31] M. S. Dutkiewicz, J. H. Farnaby, C. Apostolidis, E. Colineau, O. Walter, N. Magnani, M. G. Gardiner, J. B. Love, N. Kaltsoyannis, R. Caciuffo, P. L. Arnold, *Nat. Chem.* **2016**, *8*, 797 – 802.
[32] A. E. Reed, L. A. Curtiss, F. Weinhold, *Chem. Rev.* **1988**, *88*, 899 – 926.

[33] F. Weinhold, C. R. Landis, *Valency and Bonding: A Natural Bond Orbital Donor-Acceptor Perspective*, University Press, Cambridge, **2005**.
[34] E. D. Glendening, J. K. Badenhoop, A. E. Reed, J. E. Carpenter, J. A Bohmann, C. M. Morales, C. R. Landis, F. Weinhold, Natural Bond Order 6.0, Theoretical Chemistry Institute, University of Wisconsin, Madison, WI, **2013**. Accessed 09-01-2013.
[35] E. D. Glendening, C. R. Landis, F. Weinhold, *J. Comput. Chem.* **2013**, *34*, 1429 – 1437.
[36] D. Rios, P. X. Rutkowski, D. K. Shuh, T. H. Bray, J. K. Gibson, M. J. Van Stipdonk, *J. Mass Spectrom.* **2011**, *46*, 1247 – 1254.
[37] S. Gronert, *J. Am. Soc. Mass Spectrom.* **1998**, *9*, 845 – 848.
[38] R. G. Parr, W. Yang, *Density-Functional Theory of Atoms and Molecules*. Oxford University Press, New York, **1989**.
[39] A. D. Becke, *J. Chem. Phys.* **1993**, *98*, 5648 – 5652.
[40] C. Lee, W. Yang, R. G. Parr, *Phys. Rev. B* **1988**, *37*, 785 – 789.
[41] T. H. Dunning Jr., *J. Chem. Phys.* **1989**, *90*, 1007 – 1023.
[42] R. A. Kendall, T. H. Dunning Jr., R. J. Harrison, *J. Chem. Phys.* **1992**, *96*, 6796 – 6806.
[43] K. A. Peterson, *J. Chem. Phys.* **2015**, *142*, 074105-1-074105 – 14.
[44] M. Dolg, X. Cao, *J. Phys. Chem. A* **2009**, *113*, 12573 – 12581.
[45] A. Weigand, X. Cao, T. Hangele, M. Dolg, *J. Phys. Chem. A* **2014**, *118*, 2519 – 2530.
[46] M. Vasiliu, K. A. Peterson, J. K. Gibson, D. A. Dixon, *J. Phys. Chem. A* **2015**, *119*, 11422 – 11431.
[47] W. Küchle, M. Dolg, H. Stoll, H. Preuss, *J. Chem. Phys.* **1994**, *100*, 7535 – 7542.
[48] X. Cao, M. Dolg, H. Stoll, *J. Chem. Phys.* **2003**, *118*, 487 – 496.
[49] X. Cao, M. Dolg, *J. Mol. Struct.* **2004**, *673*, 203 – 209.
[50] Gaussian 09, Revision D.01 (**2009**), M. J. Frisch, G. W. Trucks, H. B. Schlegel, G. E. Scuseria, M. A. Robb, J. R. Cheeseman, G. Scalmani, V. Barone, B. Mennucci, G. A. Petersson, H. Nakatsuji, M. Caricato, X. Li, H. P. Hratchian, A. F. Izmaylov, J. Bloino, G. Zheng, J. L. Sonnenberg, M. Hada, M. Ehara, K. Toyota, R. Fukuda, J. Hasegawa, M. Ishida, T. Nakajima, Y. Honda, O. Kitao, H. Nakai, T. Vreven, J. A. Montgomery, Jr., J. E. Peralta, F. Ogliaro, M. Bearpark, J. J. Heyd, E. Brothers, K. N. Kudin, V. N. Staroverov, T. Keith, R. Kobayashi, J. Normand, K. Raghavachari, A. Rendell, J. C. Burant, S. S. Iyengar, J. Tomasi, M. Cossi, N. Rega, J. M. Millam, M. Klene, J. E. Knox, J. B. Cross, V. Bakken, C. Adamo, J. Jaramillo, R. Gomperts, R. E. Stratmann, O. Yazyev, A. J. Austin, R. Cammi, C. Pomelli, J. W. Ochterski, R. L. Martin, K. Morokuma, V. G. Zakrzewski, G. A. Voth, P. Salvador, J. J. Dannenberg, S. Dapprich, A. D. Daniels, O. Farkas, J. B. Foresman, J. V. Ortiz, J. Cioslowski, D. J. Fox, Gaussian, Inc., Wallingford CT.
[51] G. D. Purvis III, R. J. Bartlett, *J. Chem. Phys.* **1982**, *76*, 1910 – 1918.
[52] K. Raghavachari, G. W. Trucks, J. A. Pople, M. Head-Gordon, *Chem. Phys. Lett.* **1989**, *157*, 479 – 483.
[53] J. D. Watts, J. Gauss, R. J. Bartlett, *J. Chem. Phys.* **1993**, *98*, 8718 – 8733.
[54] R. J. Bartlett, M. Musial, *Rev. Mod. Phys.* **2007**, *79*, 291 – 352.
[55] M. Douglas, N. M. Kroll, *Ann. Phys.* **1974**, *82*, 89 – 155.
[56] G. Jansen, B. A. Hess, *Phys. Rev. A* **1989**, *39*, 6016 – 6017.
[57] A. Wolf, M. Reiher, B. A. Hess, *J. Chem. Phys.* **2002**, *117*, 9215 – 9226.
[58] K. A. Peterson, T. H. Dunning Jr., *J. Chem. Phys.* **2002**, *117*, 10548 – 10560.
[59] W. A. De Jong, R. J. Harrison, D. A. Dixon, *J. Chem. Phys.* **2001**, *114*, 48 – 53.
[60] F. Rulin, K. A. Peterson, *J. Chem. Phys.* **2017**, *147*, 084108.
[61] M. J. O. Deegan, P. J. Knowles, *Chem. Phys. Lett.* **1994**, *227*, 321 – 326.
[62] M. Rittby, R. J. Bartlett, *J. Phys. Chem.* **1988**, *92*, 3033 – 3036.
[63] P. J. Knowles, C. Hampel, H.-J. Werner, *J. Chem. Phys.* **1993**, *99*, 5219 – 5228.
[64] H.-J. Werner, P. J. Knowles, G. Knizia, F. R. Manby, M. Schütz, P. Celani, T. Korona, R. Lindh, A. Mitrushenkov, G. Rauhut, MOLPRO, version 2012.1, a package of ab initio See http programs,//www.molpro.net. Accessed 10-01-2012.
[65] H.-J. Werner, P. J. Knowles, G. Knizia, F. R. Manby, M. Schütz, *WIREs Comput. Mol. Sci.* **2012**, *2*, 242 – 253.
[66] G. te Velde, F. M. Bickelhaupt, S. J. A. van Gisbergen, C. Fonseca Guerra, E. J. Baerends, J. G. Snijders, T. Ziegler, *J. Comput. Chem.* **2001**, *22*, 931 – 967.
[67] *ADF Release 2017*, *ADF Users Guide*, https//www.scm.com/doc/ADF/downloads/ADF.pdf, SCM, Theoretical Chemistry, Vrije Universiteit, Amsterdam, accessed May 1, **2017**.
[68] E. van Lenthe, A. E. Ehlers, E. J. Baerends, *J. Chem. Phys.* **1999**, *110*, 8943 – 8953.
[69] E. van Lenthe, E. J. Baerends, J. G. Snijders, *J. Chem. Phys.* **1993**, *99*, 4597 – 4610.
[70] E. van Lenthe, E. J. Baerends, J. G. Snijders, *J. Chem. Phys.* **1994**, *101*, 9783 – 9792.
[71] E. van Lenthe, J. G. Snijders, E. J. Baerends, *J. Chem. Phys.* **1996**, *105*, 6505 – 6516.
[72] E. van Lenthe, R. van Leeuwen, E. J. Baerends, J. G. Snijders, *Int. J. Quantum Chem.* **1996**, *57*, 281 – 293.
[73] A. D. Becke, *Phys. Rev. A* **1988**, *38*, 3098 – 3100.

Manuscript received: September 6, 2017
Accepted manuscript online: October 12, 2017
Version of record online: November 10, 2017